Science Robotics
AAAS

Supplementary Materials for

Mechanical intelligence simplifies control in terrestrial limbless locomotion

Tianyu Wang *et al.*

Corresponding author: Daniel I. Goldman, daniel.goldman@physics.gatech.edu

Sci. Robot. **8**, eadi2243 (2023)
DOI: 10.1126/scirobotics.adi2243

The PDF file includes:

Other Supplementary Material for this manuscript includes the following:

Supplementary Methods

Biological experiment

Lattice setup

Micro-fluidic pillar arrays were constructed using conventional soft-lithography techniques (Fig. S1A). SU-8 molds were patterned via UV photolithography. Polydimethylsiloxane or PDMS (Dow Corning Sylgard 184) was poured onto the molds (10:1 elastomer to curing agent ratio), cured at 70°C overnight in an oven and peeled from the molds. The PDMS devices were

cut into shapes and holes for nematode loading and fluid flow were punched using a biopsy punch. Devices were then bonded to glass substrates using a handheld corona plasma treatment wand.

Microfluidic devices were first degassed using by flowing in a Pluronic and DI water mixture. Once all air was removed, the devices were flushed with flowing S-basal buffer for several minutes. Nematodes were then loaded rinsed off of their plates with S-basal, washed 3 times and loaded into a syringe. The syringe was then connected to the device and nematodes were pushed into the pillar array. The device was then sealed using capped syringe tips in the entry and exit ports and then continuously imaged for $\sim$10 minutes at 20 FPS on a dissecting scope (Leica).

Video processing

Video recordings were first cropped to isolate bouts of individual nematodes performing bouts of forward swimming/crawling behaviors (stationary nematodes were ignored). A reference image containing only the pillars was constructed by averaging the frames of an entire bout, or by selecting a frame when the nematode was out of the cropped video. Background subtraction was then performed to isolate the nematode. Thresholding was used to binarize the image of the nematode, creating a series of black and white masks. Each mask was then skeletonized to isolate the centerline. These image processing steps were performed in ImageJ. The centerlines were then converted into curvature heatmaps in MATLAB, using a B-spline to interpolate between the pixel-wise centerline points. The curvatures were then used to perform subsequent analysis using MATLAB.

Robophysical model design and manufacturing

The robophysical model was constructed as a chain of linked identical modules (Fig. S3, 7 joints and 86 cm body length). Each individual module consisted of a two-axis servo motor housed inside a case. The cases were attached to one another with a unilaterally bending joint linkage. Pulleys were then attached to each axis of the motor, and the pulleys were spooled with strings, which were referred to as cables. To complete the design, the cables were unspooled through the case and fixed onto the case ahead of the current one. Additional add-on features, such as skins and wheels, were also included for specific robophysical experiments to model the biological model.

Each module contained a Dynamixel 2XL430-W250-T servo motor (ROBOTIS), which had two axes that could be controlled independently. This feature enables the left and right cables to be adjusted to different lengths as needed. With a stall torque of 1.4 Nm, the motor provides ample support for the cable tension resulting from body-environment interactions. Additionally, the motor offers precise and continuous position control, with small enough resolution for multiple rotations. This feature allows for accurate cable length controls, where it is assumed that the cable length was approximately proportional to the motor position within the range between the maximum and minimum cable lengths.

The case that houses the servo motor serves as the main structural component and skeleton of the body. It was custom designed (55 mm length, 68 mm diamater) and manufactured to fit the motor's geometry and was 3D printed (Raise3D E2 3D printer) using PLA material. To attach the case to other components, such as the joint and wheels, heat-insets were inserted into all the holes. All the cases were identical, except for the one at the anterior end (head) of the robophysical model, which had a rounded shape for smoother head-obstacle interactions.

The joint (28 mm length) connecting adjacent modules in our system provides one degree of freedom rotation, with the axis of rotation perpendicular to the ground surface. We 3D printed

joints with PLA material. Each joint allows a full range of 180 degrees of rotation, from -90 to $+90$ degrees, with the neutral position at 0 degrees where the two links align. The joints are secured to the cases with two screws that connect directly to the heat insets, facilitating easy rearrangement and replacement.

The cables are the component that drives the movement of the robophysical model. To achieve this, we utilized nonelastic fishing lines (Rikimura) that boast high tensile strength of up to 180 pounds and demonstrate negligible deformation and shape memory upon stretching. To control the shortening and lengthening of the cables, we employed pulleys (9.5-mm diameter) that were 3D printed using PLA material and attached to each rotational shaft of the servo motor. One end of each cable was fixed to the pulley, whereas the rest was tightly wound around it. This configuration allows the length of the cable to vary proportionally with the rotation angle of the pulley, which can be accurately controlled by the servo motor. The other end of each cable was threaded through a small guiding hole on the edge of the case and attached to the other case linked by the joint. For each joint, two cables were present on either side, controlling the full range of motion of the joint. A cable shortens when it is taut and under tension, whereas it lengthens when it is slack and has no tension.

Our robophysical model was controlled using code developed with the Dynamixel SDK library and programmed in MATLAB. Control signals were transmitted to the robophysical model from a PC via U2D2 (ROBOTIS). We powered the motors using a DC power supply (HY3050EX) with a voltage setting of 11.1 V. As the servo motors were connected in a daisy chain configuration for both power and communication, we connected the U2D2 and power supply to the last motor in the series.

We used an elastic mesh sleeve (1.75-inch ID polyester fabric expandable sleeving, McMaster-Carr) to wrap around the robophysical model body. Note that the sleeve cannot create anisotropy to provide any extra propulsion. The benefit of using an isotropic sleeve is twofold. The robo-

physical model is made of discretized hard modules and joints; therefore, it can get wedged unexpectedly in the heterogeneities because of the irregular structures, such as edges of the case. The sleeve can smooth the discretization of the body to allow for more continuous body contact with the environment. The sleeve also provides weak passive elasticity, facilitating a weak but inherent "potential" for the robophysical model to return to the straight posture. This elasticity was found helpful especially in the passive behaviors that the robophysical model displayed and share similarities with those in biological model. The force effect of the sleeve was also considered when the force-deformation properties of the robophysical model were characterized.

The wheels are attachable components that can be attached or removed from the bottom of each case. To attach wheels onto the case, a base was 3D printed using PLA and screwed to the base. Then, the wheel frame (LEGO) was screwed into the base. The wheels were passive, non-actuated. To achieve a similar drag anisotropy for the robophysical model as for the biological model ($\sim 1.5:1$), we replaced the rubber tires with low-friction fiberglass tape (McMaster-Carr), resulting in a $1.6:1$ drag anisotropy ($F_{\perp}/F_{\parallel} = 1.6/1$, verified with wheel force experiments following the protocols proposed in (*89*)). This allowed us to better model the low Reynolds number viscous fluid locomotion of the biological model. Noted that in open and sparse environments, wheels are necessary for the robophysical model to produce propulsion with drag anisotropy. However, as heterogeneity density increases, the propulsion forces provided by pushing off heterogeneity generally dominates the locomotion, and the robophysical model can move forward effectively without wheels. For consistency in the experimental setup and comparison with the biological model, we kept the wheels on for robophysical experiments in all environments.

The head collision sensor is an add-on structure in the closed-loop robophysical model, for studying how mechanical intelligence can be imposed by active reversal behaviors and modeling

the head sensing neurons of *C. elegans*, we designed and 3D printed a head for the robophysical model that is capable of sensing the collision angle (discrete) and the rough magnitude of collision forces. Five force-sensing resistors (FSR, Interlink Electronics FSR Model 408) were attached in parallel on the curved head surface (Fig. 7C). The feedback analog signals were collected using an Arduino micro-controller (Seeeduino XIAO SAMD21). The collision angle ranges that each FSR can detect are roughly 65° to 75°, 75° to 85°, 85° to 95°, 95° to 105° and 105° to 115°. The thresholds that we set to trigger the reversal behavior in the closed-loop control of the robophysical model were 3 N for the third (the middle) FSR and 5 N for the second and forth (left and right middle) FSR. When the head collision sensor sensed collision force beyond the set thresholds, the robophysical model was programmed to initiate a reversal behavior, where we fixed the reverse duration to be 0.125 cycle so that we focus on studying the effect of reversals, despite that the duration of nematode reversals was observed to vary from 0.1 to 2 cycles.

Robophysical model control

We calculated the exact lengths of the left and right cables that can form a joint angle α, $\mathcal{L}^l(\alpha_i)$ and $\mathcal{L}^r(\alpha_i)$, based on the geometry of the joint mechanical design (Fig. S4). "Exact length" means the cable is in a shortened state, forming a straight line. Thus, $\mathcal{L}^l$ and $\mathcal{L}^r$ follow

$$\begin{aligned}\mathcal{L}^l(\alpha_i) &= 2\sqrt{L_c^2+L_j^2}\cos\left[-\frac{\alpha_i}{2}+\tan^{-1}\left(\frac{L_c}{L_j}\right)\right],\\ \mathcal{L}^r(\alpha_i) &= 2\sqrt{L_c^2+L_j^2}\cos\left[\frac{\alpha_i}{2}+\tan^{-1}\left(\frac{L_c}{L_j}\right)\right].\end{aligned} \tag{S1}$$

Considering design parameters of our robophysical model, we have

$$\begin{aligned}\mathcal{L}^l(\alpha_i) &= 79.2\cos\left(-\frac{\alpha_i}{2}+\frac{\pi}{4}\right)\text{mm},\\ \mathcal{L}^r(\alpha_i) &= 79.2\cos\left(\frac{\alpha_i}{2}+\frac{\pi}{4}\right)\text{mm}.\end{aligned} \tag{S2}$$

We followed Eq. 3 to control the lengths of the left and right cables $L_i^{l/r}$ for the i-th joint.

We converted the linear motion of shortening and lengthening cables to the rotary motion of pulleys by spooling cables onto them. Since arc length is proportional to the center rotational angle, which we can directly control via servo motor (4096 positions per full rotation, 0.088° resolution), we commanded the motor position P to achieve the shortening and lengthening of cable length L using

$$P(L) = P_0 - \gamma L, \tag{S3}$$

where P_0 is the position of the motor when the cable length is 0 (calibrated for each cable), and $\gamma = \frac{\text{Motor positions per full rotation}}{\text{Cable coil length per full rotation}} = \frac{4096}{\pi D_{\text{pulley}}} = 137.2$ mm^{-1}. Note that $L \geq 0$ and we regulated the positive direction of motor rotation corresponds to the shortening of the cable, according to our mechanical design, thus P_0 is the maximum motor position and γ is positive. Also note that, we neglected the change of pulley radii due to the thickness of the cable (< 0.5 mm). By substituting Eq. 3 into Eq. S3, we obtained the control policy in terms of motor position that we directly programmed to run the robophysical model. Practically, we set γl_0 to be a constant with a magnitude of 100 throughout this work, yielding $l_0 = 0.73$ mm/degree.

By varying the value of generalized compliance G, the robophysical model can display different levels of body compliance and mechanical intelligence, allowing the robophysical model to implement specific kinematics (gaits from nematodes) while passively mediate and respond to environmental perturbations. Fig. S5 provides a detailed explanation of the behaviors that one single joint and the whole robophysical model can display when G falls in different ranges. The first schematic in each row shows the state of the joint (either bidirectionally non-compliant, directionally compliant, or bidirectionally compliant) and the state of left and right cables (either shortened or lengthened) depending on which region the suggested joint angle falls into. The second plot in each row illustrates the actual lengths comparing with the exact lengths of left and right cables on either sides of the joint as a function of the suggested joint angle, where overlaps of actual and exact lengths means the cable is shortened, whereas the

discrepancy between actual and exact lengths shows how much the cable is lengthened. Note that $\mathcal{L}(0)$ on the y-axis means the exact length of a cable when joint angle is 0, $\mathcal{L}_{\text{max}}$ and $\mathcal{L}_{\text{min}}$ mean the exact length of the left (right) cable when the joint angle is 90° and -90° (-90° and 90°), respectively. The third plot in each row illustrates the feasible range of all possible emergent joint angle, showing how much a single joint angle could depart the suggested joint angle by perturbation of external forces, enabled by lengthening of cables. The last figure in each row depicts the feasible region of all possible emergent gait paths of the robophysical model, taking all joints as a whole, in the shape space spanned by w_1 and w_2. We projected the collection of upper bounds for all joints onto the $\sin$ and $\cos$ shape basis functions to acquire the outer bound of the possible gait paths. And similarly we projected lower bounds of joint angle to acquire the inner bound of the possible gait paths. The region bounded by inner and outer bounds then illustrates how much the robophysical model could depart the suggested gait path by perturbation of external forces.

Note that although the three representative values of G ($G = 0, 0.5, 1$) are not related to the robophysical model's geometry and gait parameter selection, the fully passive value, the value over which G exceeds the robot will become fully passive, is related to the geometry and parameter selection. The accurate fully passive value can be calculated using the forth equation given in Eq. 3,

$$\mathcal{L}^r[A \cdot \min(1, 2G - 1)] + l_0 \cdot [(2G - 1)A - A] = \mathcal{L}_{max}, \tag{S4}$$

meaning that when the commanded angle is set to the maximum amplitude ($\alpha = A$), the right cable is loosened to the maximum length such that the joint can freely bend to the minimum amplitude ($-A$); thus the joint is fully passive. Note that without the loss of symmetry, using the left cable equation (the second equation in Eq. 3) will lead to the same result. Given $G > 0.5$,

it can be simplified as

$$\mathcal{L}^r(A) + 2l_0A(G-1) = \mathcal{L}_{max}. \tag{S5}$$

Solve for G, we get $G = 1 + \frac{\mathcal{L}_{max}-\mathcal{L}^r(A)}{2l_0A}$, the fully passive value as shown in Fig. S5. $\mathcal{L}_{max}$ and $\mathcal{L}^r(A)$ can be directly calculated using Eq. S2, by letting $\alpha = \pi/2$ and $\alpha = A$. Thus, in this work, substituting in the amplitude parameters we test ($A = 46°, 48°, 51°, 72°$) and $l_0 = 0.73$ mm/degree, the exact fully passive values are $G = 1.74, 1.73, 1.71, 1.64$, respectively. Considering in the robophysical experiments we varied G value with a 0.25 interval, $G = 1.75$ works as a general approximated fully passive value throughout the work.

Robophysical kinematics analysis and comparison

We describe the kinematics of nematodes using their curvature profile (Fig. S6), calculated from images as described before. The local curvature is defined as $\kappa(s) = \frac{1}{r(s)}$ where s is the body coordinate increasing from head to tail.

Undulatory waves in nematodes may be approximated by a serpenoid wave (*62*) where the curvature is a traveling wave:

$$\kappa(s,t) = A\sin(\omega t + ks), \tag{S6}$$

where $\kappa(s,t)$ is the local curvature evaluated at time t and arc-length s; ω is the temporal frequency and k is the spatial frequency. While nematodes and other organisms are continuous, robots including our robophysical model are generally made from a small number of discrete components. To understand how the shapes of a discrete jointed undulator map onto a continuously curving undulator, we first consider the curvature of a continuous undulator evaluated at a discrete set of points along body, in which case Eq. S6 can be written as

$$\kappa(i,t) = A\sin(\omega t + k_d i), \tag{S7}$$

where i is the index of discretized points.

We further decompose the serpenoid traveling wave into the product between temporal component and spatial component:

$$\begin{aligned}\kappa(i,t) &= \underbrace{A\sin(\omega t)}_{w_1(t)}\underbrace{\cos(k_d i)}_{\beta_1(i)} + \underbrace{A\cos(\omega t)}_{w_2(t)}\underbrace{\sin(k_d i)}_{\beta_2(i)} \\ &= w_1(t)\beta_1(i) + w_2(t)\beta_2(i),\end{aligned} \tag{S8}$$

where $\beta_1(i)$ and $\beta_2(i)$ are time-invariant shape-basis function to prescribe a serpenoid traveling wave.

Now we consider applying the serpenoid curve to a robophysical model with discretized joints and links. Define $\vec{T}(i)$ to be the tangent vector evaluated at i-th points along the curve. Note that $\vec{T}(i)$ has unit length, $|\vec{T}(i)| = 1$. Let $\vec{T}(i+1)$ be the unit tangent vector evaluated at $(i+1)$-th point. The distance between two consecutive points should be $\Delta s = L/N$, where L is the total length of the curve and N is the total number of points. Notably, $\kappa(i)$ is defined as

$$\kappa(i) = \lim_{N\to\infty} \frac{|\vec{T}(i+1) - \vec{T}(i)|}{\Delta s}. \tag{S9}$$

We define $\alpha(i)$ as the joint angle between the tangent vector $\vec{T}(i+1)$ and $\vec{T}(i)$. From geometry, we have

$$|\vec{T}(i+1) - \vec{T}(i)| = |\Delta\vec{T}| = 2\sin(\alpha(i)/2). \tag{S10}$$

Substituting into Eq. S9, we have

$$\kappa(i) = \lim_{N\to\infty} \frac{2\sin(\alpha(i)/2)}{L/N}. \tag{S11}$$

Since $\lim_{N\to\infty} 2\sin(\alpha(i)/2) = \alpha(i)$, we have $\kappa(i) = N\alpha(i)/L$ as $N \to \infty$. Thus, in a discretized case (in our case, a robophysical model), joint angle is a reasonable alternate variable to curvature in the continuous case to describe kinematics,

$$\alpha(i,t) = w_1(t)\beta_1^\alpha(i) + w_2(t)\beta_2^\alpha(i), \tag{S12}$$

as in Eq. 2. Therefore, in a general sense, joint angles of the robophysical model and the body curvatures of the nematode are comparable quantities, as well as their gait paths in the shape space (as shown in Fig. 2A and Fig. 4A). More generally, continuous curvature can be mapped onto to the discrete joint angle representation of gaits. In the limit of infinite link numbers they are fully equivalent, but for finite joint numbers they coincide with points along the continuous body and only diverge between the joints.

Supplementary Discussion

Coasting numbers for biological and robophysical models

We consider fluid-swimming nematode locomotion occurs in a sufficiently low Reynolds number environment ($\sim$0.1), which permits the valid assumption of inertialess locomotion. Notably, when a nematode ceases self-deformation, its locomotory speed decays to half of its steady-state velocity in approximately 5 ms, primarily due to viscous Stokes drag (*92*). We refer this period as the "coasting time," denoted as τ_{coast}, and introduce the dimensionless "coasting number" (*56*), $\mathcal{C} = 2\tau_{\text{coast}}/\tau_{\text{cycle}}$, where τ_{cycle} denotes the gait period, and $\tau_{\text{cycle}} \approx 1$ s for nematodes. Thus, $\mathcal{C}$ for nematodes is $\sim$0.01.

We can apply the concept of inertialess locomotion to the robophysical model. To justify this extension, we assess the ratio of inertial to frictional forces in Coulomb friction-dominated systems using: $\mathcal{C} = \frac{mv_0/\tau_{\text{cycle}}}{\mu mg}$, where m, v_0, τ_{cycle}, μ and g are body mass, average locomotion speed, temporal gait period, friction coefficient and gravitational acceleration constants respectively. Simplifying, we obtain $\frac{v_0/(\mu g)}{\tau_{\text{cycle}}}$, where the numerator can be interpreted as the time required to go from steady-state locomotion to a complete stop. In frictional fluid environments, where force is approximately rate-independent, we have $\tau_{\text{coast}} = \frac{1}{2}v_0/(\mu g)$. In this context, this ratio for the robophysical model is then exactly $\mathcal{C}$ for nematodes. And for the robophysical model $\mathcal{C}$ is sufficiently small (on the order of 0.001), which allows us to disregard inertial effects and

compare its locomotion to that of nematodes.

Robot performance in diverse environments

Evaluation metrics and methods

In addition to the wave efficiency η (which is the ratio of the center of mass velocity to the wave propagation velocity) that we used to describe the robot's locomotion speed, we also calculated the mechanical cost of transport c_{mt}. This dimensionless quantity, widely used in the study of legged animals and robots (*27, 93–95*), gives the work required to move a unit body weight a unit distance and allows us to analyze the robot's locomotion efficiency in a more comprehensive manner.

To calculate the mechanical cost of transport, we used the formula $c_{\text{mt}} = W/mgd$, where W is the work done by cables, mg is the robot's weight, and d is the distance traveled. We estimated the tension T exerted by each cable using the torque sensor embedded in the servo motor (ROBOTIS 2XL430-W250-T). During an experiment, we recorded the torque readings τ from the motor with a time interval of $\Delta t = 10$ ms. To obtain the nominal torque readings τ_0, which represent the "metabolic" torques required to enable the shaft to rotate without moving the robot, we ran a calibration experiment with the same motor running the same trajectory without tying the cable to the pulley. We then estimated the tension at each time step using the formula $T = (\tau - \tau_0)/R_{\text{pulley}}$, where R_{pulley} is the radius of the pulley. To estimate the distance traveled Δl, we measured the rotation angle difference $\Delta\zeta$ of the servo motor via its internal encoder within the time interval Δt times R_{pulley}. By summing up the products of the tension and distance for each time step, we calculated the work done by one cable during an experiment. We then summed up the work done by all cables to obtain the total work done by cables. The traveled distance d was measured using tracking data by summing up the distance traveled by the robot's center of geometry during each time interval.

Flat ground

Fig. S12A shows the robot's wave efficiency η and mechanical cost of transport c_{mt} on a wood-surface flat ground, where the robot was equipped with wheels to generate a $\sim$1.6:1 drag anisotropy and move forward with retrograde wave propagation along the body. Gait parameters were fixed as $A = 46^\circ$ and $\xi = 0.82$ as discussed in Materials and Methods. As the generalized compliance G increases, we observed a nearly proportional decrease in η and increase in c_{mt}. We omitted data points where $c_{\text{mt}} > 20$ in all the plots. The robot's performance on the flat ground serves as a benchmark for comparison with other environments that we tested.

Granular media

As demonstrated in previous work, a limbless robot can generate forward thrust in granular media with retrograde wave (*73, 96*), thus the robot was not equipped with wheels for tests in granular media. The experiments were conducted in a pool of plastic spheres with a diameter of 5 mm, which could not enter the motor and potentially damage the robot. Gait parameters were fixed as $A = 60^\circ$ and $\xi = 1$. At the range of $0 \leq G \leq 1$, η shares a similar decreasing trend as on the flat ground (Fig. S12B). Surprisingly, we observed a more dramatic decrease in the work done by cables, yielding a decreasing c_{mt} with a local minima at $G = 0.75$. From this result we posit that, with lower body compliance, much of the active work done by the robot cannot effectively transfer into thrusting forces in such environments, and is wasted instead. By increasing the body compliance to let the robot "flow" with the environment (react to it), we reduce energy consumption without sacrificing locomotion speed. However, when G is too high, the locomotion speed drops notably, leading to an increase in c_{mt}. Such a result suggests that by leveraging the mechanical intelligence in locomotion, the robot has the potential to move efficiently within granular media.

Channel

Channels were set up to function as models for pipes and other environments where body shapes of the robot in lateral direction are highly constrained. Previous work has modeled and demonstrated that a limbless robot can gain thrust forces purely from its interactions with walls without the need of wheels for creating drag anisotropy (*74*). Differing from nematodes using retrograde waves to move in channels (*97, 98*) where we posit their thrusts primarily result from the drag anisotropy of the fluid interactions, the robot with isotropic friction needs to use direct waves to produce forward motion, solely through forces experienced on the wall. In our experiments, the robot was not equipped with wheels and we commanded the robot with a direct wave (change "$-$" into "$+$" in Eq. 2) with parameters $A = 60^\circ$ and $\xi = 1$. Specifically, the width of the robot body while employing this gait was measured as 23 cm. To make the channel a challenging environment, we set the width of the channel as 18 cm such that the robot need to "squeeze" its body to adapt to it, which is usually the case in applications such as pipe inspection. As a result (Fig. S12C), our robot cannot fit into the environment until $G = 1$. When $G \geq 1$, the robot generated effective forward locomotion in the channel and the local minima of c_{mt} emerged at $G = 1.25$. This result suggests that the generalized compliance G enables spontaneous shape adaptation to the channel without the need of probing channel width in advance, and reduced c_{mt} meanwhile. Notably, this conclusion holds true even for a wheeled limbless robot employing a retrograde wave with drag anisotropy.

Lattice

In addition to η that has been reported in the main text for the robot in regular lattices with varied density of obstacles, we evaluated c_{mt} for all experiments (Fig. S12D to E). As introduced in Materials and Methods, the robot was in the same condition as in experiments on the flat ground (with wheels), and executing open-loop gaits with fixed parameters obtained

from direct fitting from nematode kinematics in biological experiments, $A = 48°, 51°, 72°$ and $\xi = 0.80, 0.58, 1.02$ in sparse, medium and dense lattices, respectively.

Firstly, the obstacles in the sparse lattice impede locomotion of the robot with low G, resulting in reduced η compared to that on the flat ground. However, with an increasing G, the more compliant robot emerged to utilized the obstacles to generate thrust by pushing off of them, leading to an improved η, known as obstacle-aided locomotion. The local minimum of c_{mt} emerged at $G = 0.75$, where we observed both increased locomotion speed and decreased energy consumption compared to lower G values.

In the medium lattice, the robot started to become "stuck" on obstacles, where the robot cannot traverse the lattice with the commanded gait while the body was relatively rigid ($G = 0$ and 0.25). However, under the same open-loop control for the basic pattern of head-to-tail wave propagation, locomotion emerged when the body was more compliant, where η and c_{mt} also reached their maximum and minimum in the range of $0.5 \leq G \leq 1$. When the body is too compliant ($G > 1$), the robot cannot generate sufficient thrust, leading to a dramatic drop in η and increase c_{mt}.

In our experiments, we observed a similar result in the dense lattice, where only intermediate values of G led to effective and efficient locomotion. Interestingly, we also noted a slight shift in the effective range of G from $0.5 \leq G \leq 1$ (medium lattice) to $0.75 \leq G \leq 1.25$ (dense lattice). We posit that, with lower G values, the robot is better able to generate thrust by utilizing drag anisotropy, but may struggle with adapting to the environment. On the other hand, with higher G values, the robot is more compliant to the environment, but may have reduced capabilities for generating thrust (as also demonstrated by the flat ground data). As the obstacle density increases from medium to dense lattice, the constraints on body shapes become stronger, requiring the robot to be more compliant. On the other hand, in such environments, the contact forces between the robot body and the obstacles play a more dominant role in the

robot's forward motion, surpassing the contribution of drag anisotropy (as evident from the robot's ability to move in the dense lattice without wheels). Therefore, higher values of G are preferred in denser lattices, which explains the slight shift in the effective range of G from the medium lattice to the dense lattice.

Further discussion

In summary, our findings indicate that in highly constrained environments where interactions between the robot body and the environment play a dominant role in locomotion, an intermediate range of generalized compliance ($0.75 \leq G \leq 1.25$) enables the robot to be compliant enough to adapt to the environment, while minimizing the work required to maintain the wave propagation pattern. This results in local minima of c_{mt}, indicating an optimal balance between compliance and wave propagation efficiency. This insight sheds light on the importance of generalized compliance in enabling effective locomotion in challenging environments such as non-movable obstacles in medium/dense lattices and channels, where the robot needs to adapt its body shape to the environment while minimizing energy expenditure.

Supplementary Figures

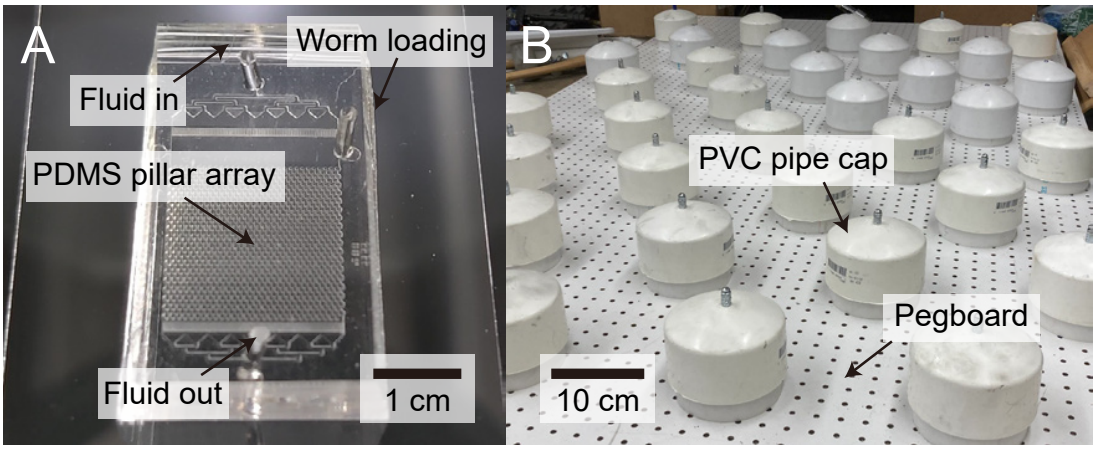

Fig. S1: Heterogeneous environments for investigating mechanical intelligence in limbless locomotors. (**A**) A microscopic pillar array for studying locomotion of *C. elegans*. (**B**) A macroscopic obstacle terrain for studying locomotion of the robophysical model.

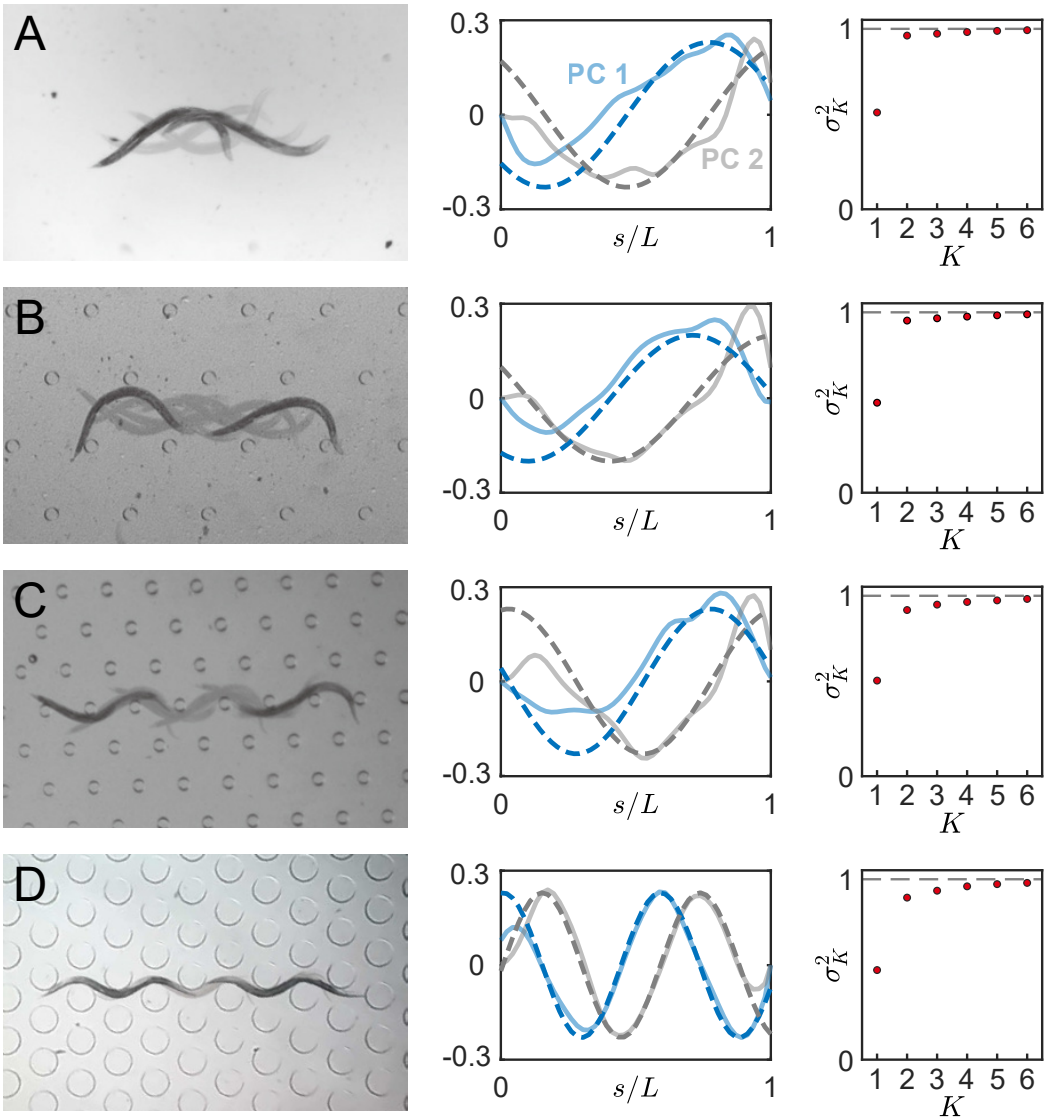

Fig. S2: Overlaid photos of *C. elegans* movements, their low dimensional representations (principal components and shape-basis functions), and total variance explained by each principal component in (**A**) open fluid, (**B**) a sparse lattice, (**C**) a medium lattice, and (**D**) a dense lattice. In the second column, solid lines are the first two dominant PCA modes of the body curvature profile and dashed lines are their best fits to sin and cos functions. Plots in the third column show the total variance explained as a function of the number of PCs.

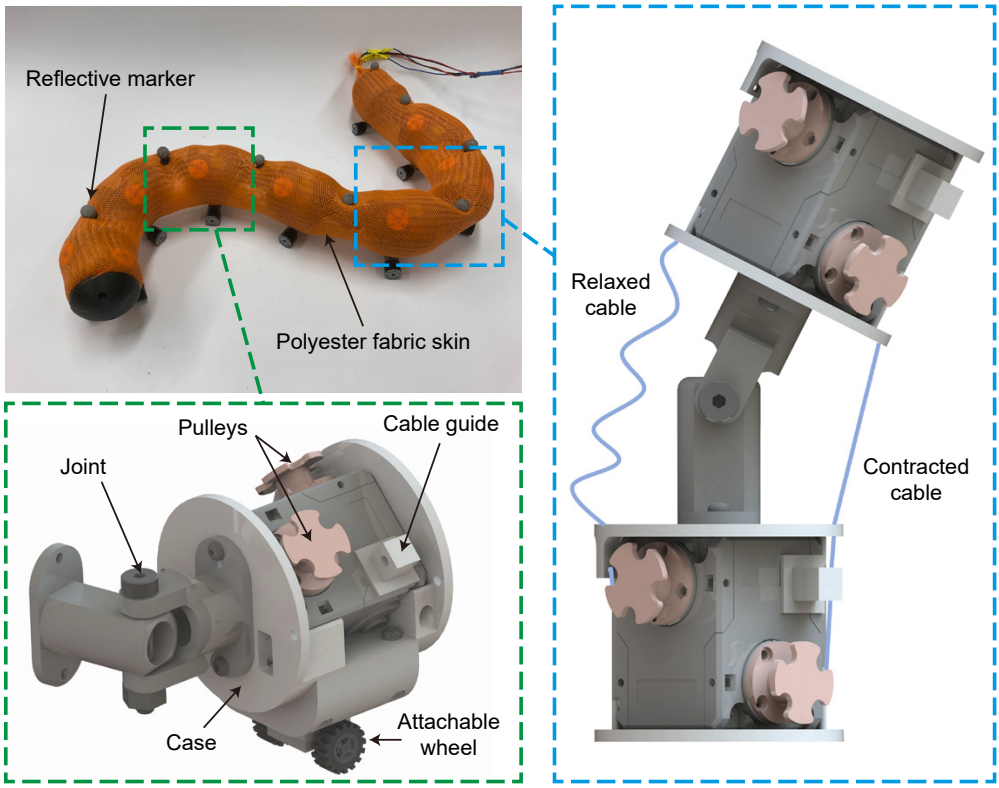

Fig. S3: A photo and computer aided design drawings detailing components of the robophysical model.

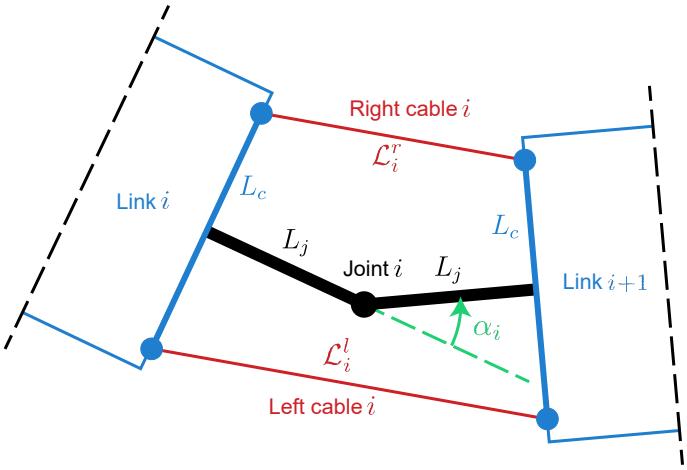

Fig. S4: Geometry of the joint mechanical design for the calculation of exact lengths of cables $\mathcal{L}_i^l$ and $\mathcal{L}_i^r$ to strictly form a suggested angle α_i.

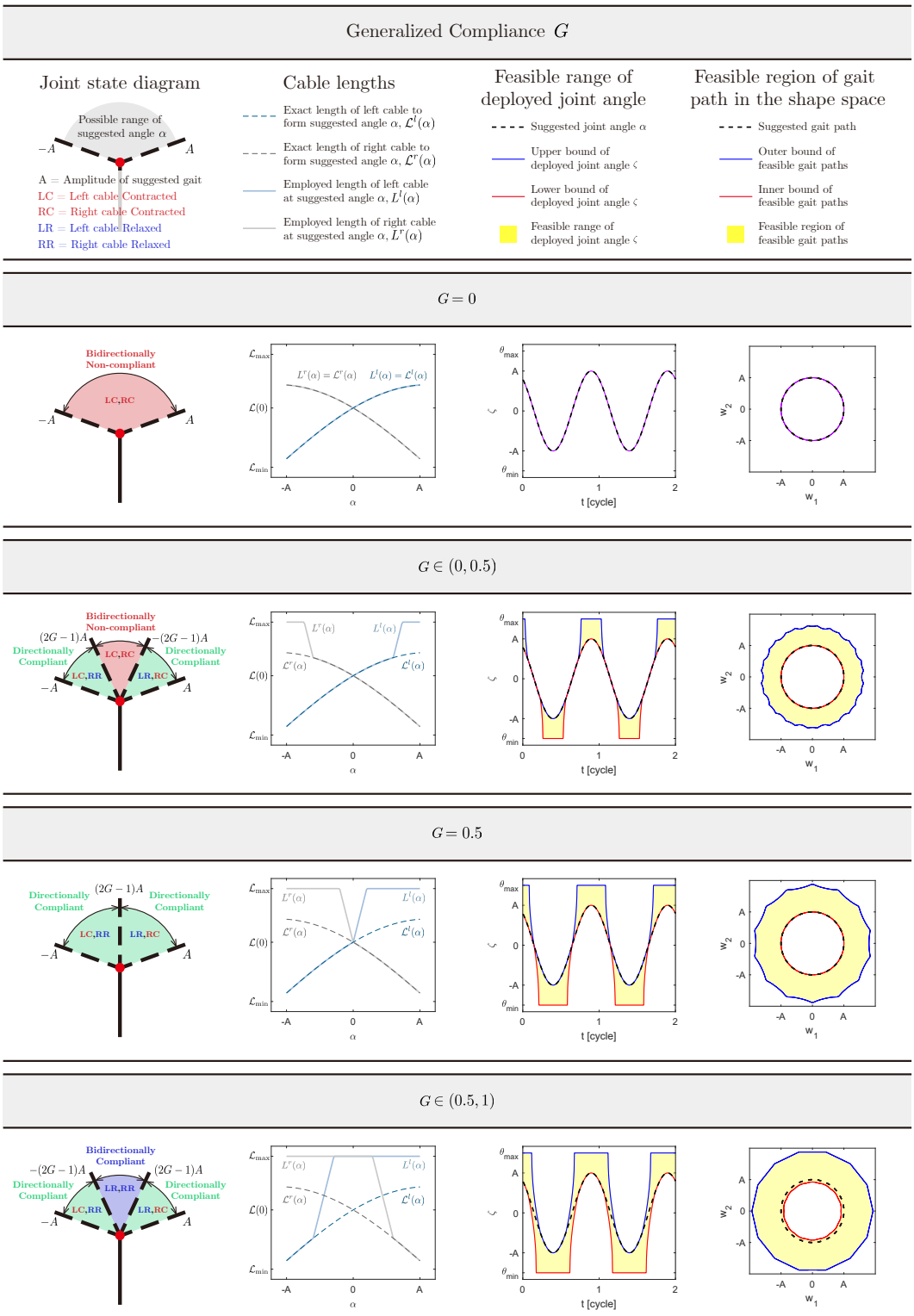
Generalized Compliance G
Joint state diagram
Possible range of suggested angle α
$-A$
A
A = Amplitude of suggested gait
LC = Left cable Contracted
RC = Right cable Contracted
LR = Left cable Relaxed
RR = Right cable Relaxed
Cable lengths
Exact length of left cable to form suggested angle α, $\mathcal{L}^l(\alpha)$
Exact length of right cable to form suggested angle α, $\mathcal{L}^r(\alpha)$
Employed length of left cable at suggested angle α, $L^l(\alpha)$
Employed length of right cable at suggested angle α, $L^r(\alpha)$
Feasible range of deployed joint angle
Suggested joint angle α
Upper bound of deployed joint angle ζ
Lower bound of deployed joint angle ζ
Feasible range of deployed joint angle ζ
Feasible region of gait path in the shape space
Suggested gait path
Outer bound of feasible gait paths
Inner bound of feasible gait paths
Feasible region of feasible gait paths
$G = 0$
Bidirectionally Non-compliant
LC,RC
$G \in (0, 0.5)$
$(2G-1)A$
Directionally Compliant
LC,RR
LR,RC
$G = 0.5$
$G \in (0.5, 1)$
Bidirectionally Compliant
LR,RR
α
t [cycle]
w_1
w_2

(Con'd)

$G = 1$			
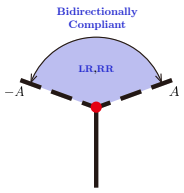	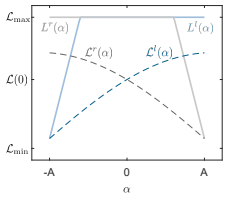	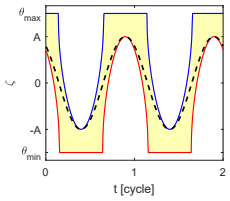	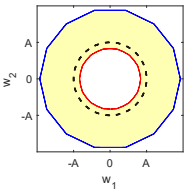
$G \in \left(1, 1 + \dfrac{\mathcal{L}(0) - \mathcal{L}^r(A)}{2l_0 A}\right)$			
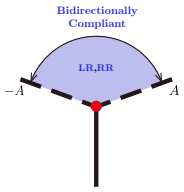	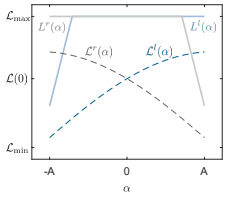	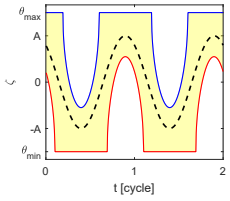	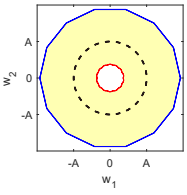
$G = 1 + \dfrac{\mathcal{L}(0) - \mathcal{L}^r(A)}{2l_0 A}$			
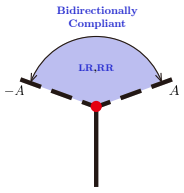	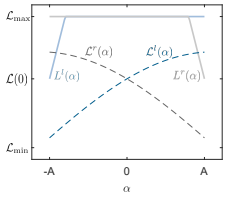	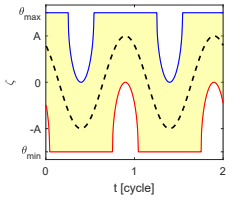	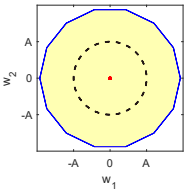
$G \in \left(1 + \dfrac{\mathcal{L}(0) - \mathcal{L}^r(A)}{2l_0 A}, 1 + \dfrac{\mathcal{L}_{\max} - \mathcal{L}^r(A)}{2l_0 A}\right)$			
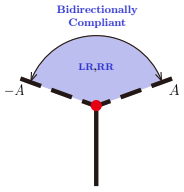	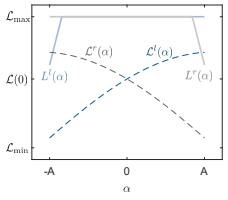	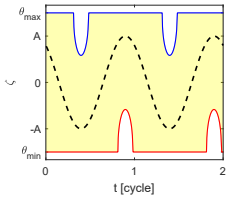	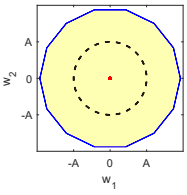
$G \in \left[1 + \dfrac{\mathcal{L}_{\max} - \mathcal{L}^r(A)}{2l_0 A}, +\infty\right)$			
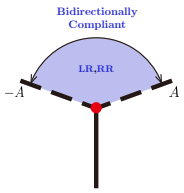	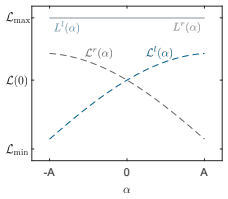	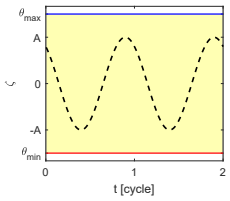	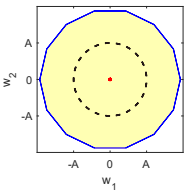

Fig. S5: An overview of behaviors that one single joint and the whole robophysical model can display with varied generalized compliance value G. The first schematic in each row shows the state of the joint, left and right cables depending on which region the suggested joint angle falls into. The second plot in each row illustrates the actual lengths according to the control scheme comparing with the exact lengths of left and right cables on either sides of the joint as a function of the suggested joint angle. The third plot in each row illustrates the feasible range of all possible emergent joint angle, showing how much a single joint angle could deviate from the suggested joint angle by perturbation of external forces. The last figure in each row depicts the feasible region of all possible emergent gait paths of the robophysical model in the shape space.

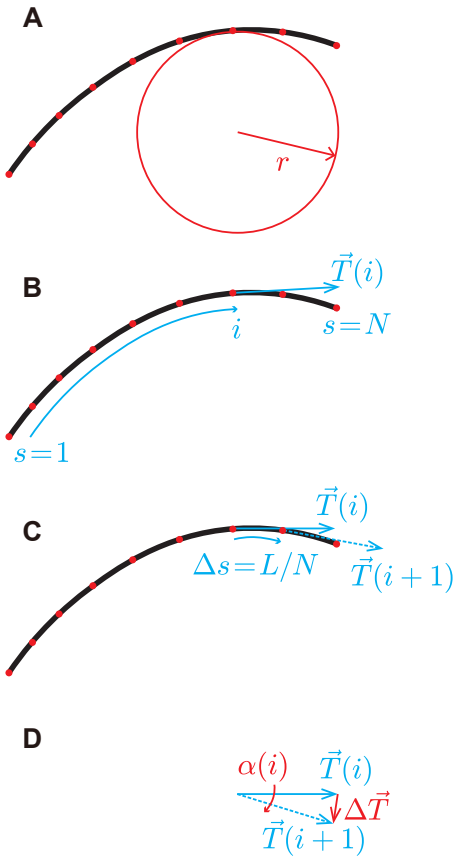

Fig. S6: Curvature estimation to demonstrate how discretization scheme reduces to curvature. (a) Discretization of a continuous curve and estimating the radius of curvature. (b) Tangent vector evaluated at the i-th point. (c) Tangent vector evaluated at the $(i+1)$-th point and the distance between two consecutive points. (d) The geometry to obtain the distance between two consecutive tangent vectors.

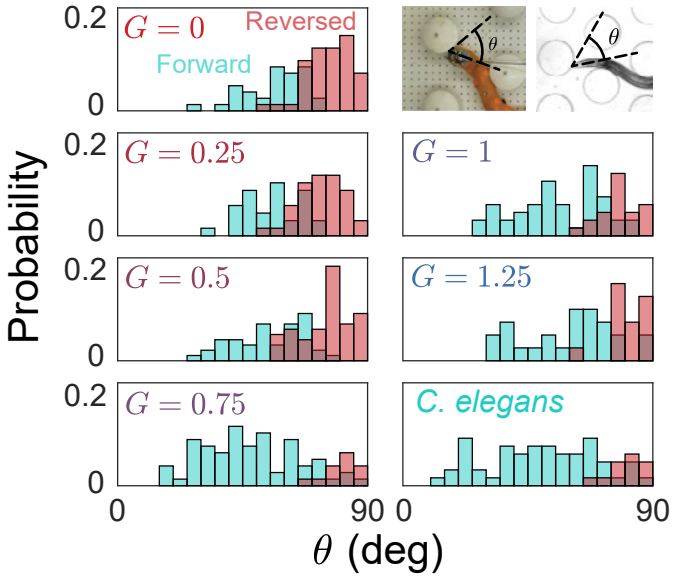

Fig. S7: Head collision angle probability distributions categorized by post-collision motion directions (forward or reversed) in the robophysical model with varied G, comparing to *C. elegans* (for each plot, sample size > 100), where the robophysical model with $G = 0.75$ closely captures *C. elegans* behaviors.

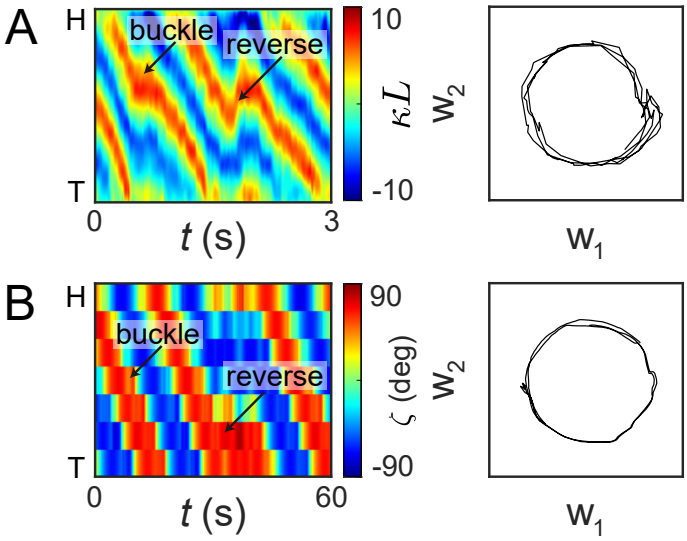

Fig. S8: Similar body kinematics displayed by (**A**) C. elegans and (**B**) the closed-loop robophysical model with $G = 0.75$ in dense lattices, by comparing body curvature (emergent joint angles) heatmaps and gait trajectories in the shape space.

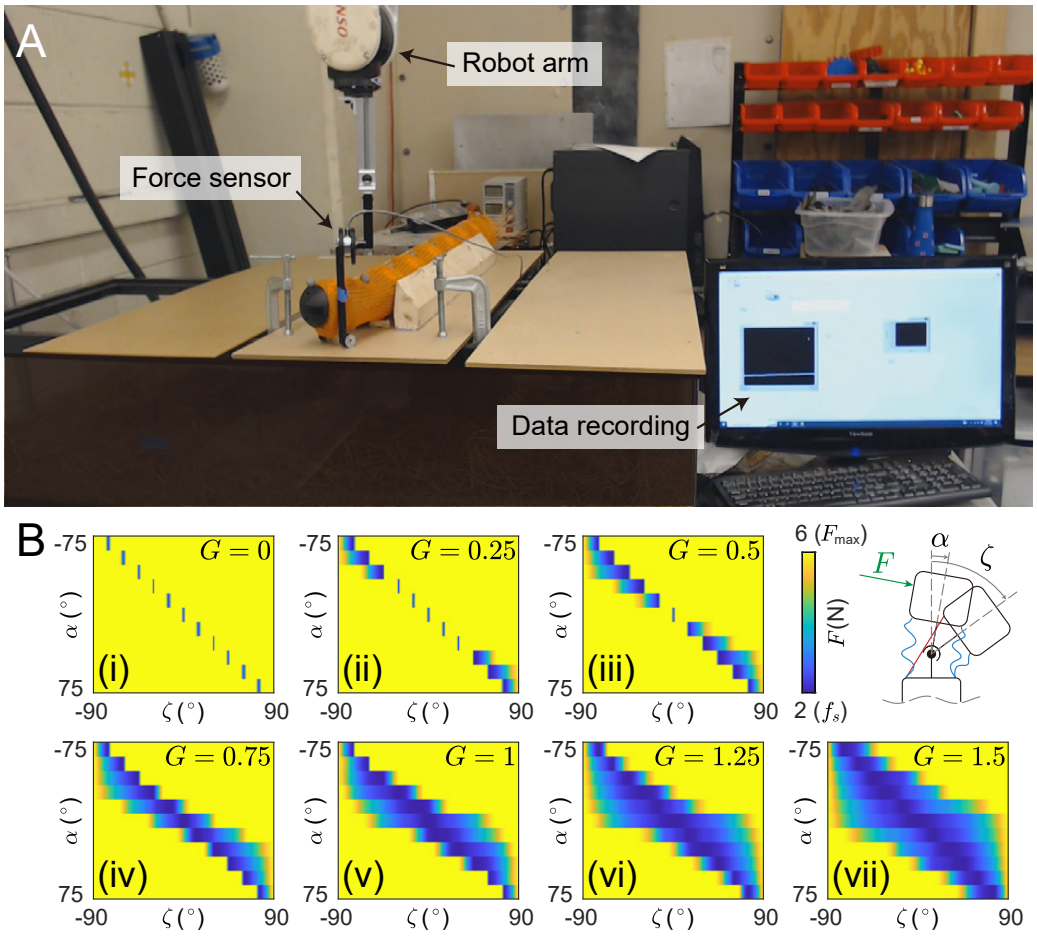

Fig. S9: Force-deformation property characterization for the robophysical model. (**A**) The experiment setup. (**B**) Force-deformation heatmaps for the robophysical model with varied G, indicating the robophysical model as a programmable functional smart material.

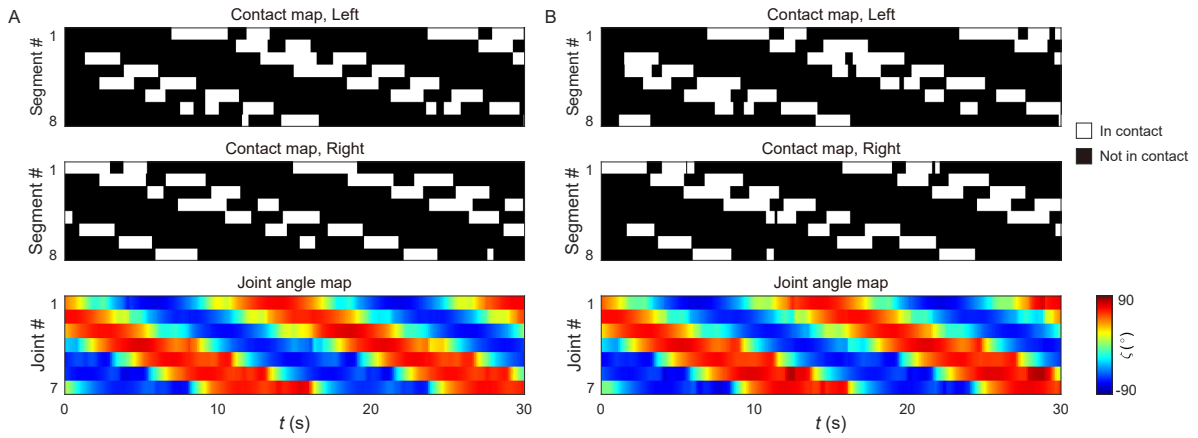

Fig. S10: Lattice collisions match the symmetry of the gait. Contact maps and curvature map for a wheeled (A) and wheelless (B) robot, both with $G = 0.75$. Contact maps of collisions of the robot and lattice points on the left (top row) and right (middle row) side of the body show at what body point and at what times contact with the lattice occurs (contact shown in white, absence of contact in black). These contact patterns show similar patterns to the gait, as visualized in a curvature map (bottom row) with collisions on the left-hand side of the robot corresponding with regions of positive curvature and right-hand side collisions with negative curvature. Wheeled and wheelless robots show qualitatively similar contact patterns, highlighting the dominance of lattice collisions in producing thrust (relative to ground contact) in dense lattices. Note that the head often shows longer durations of contact relative to the rest of the body, a result of the dynamics of buckling and gliding collisions.

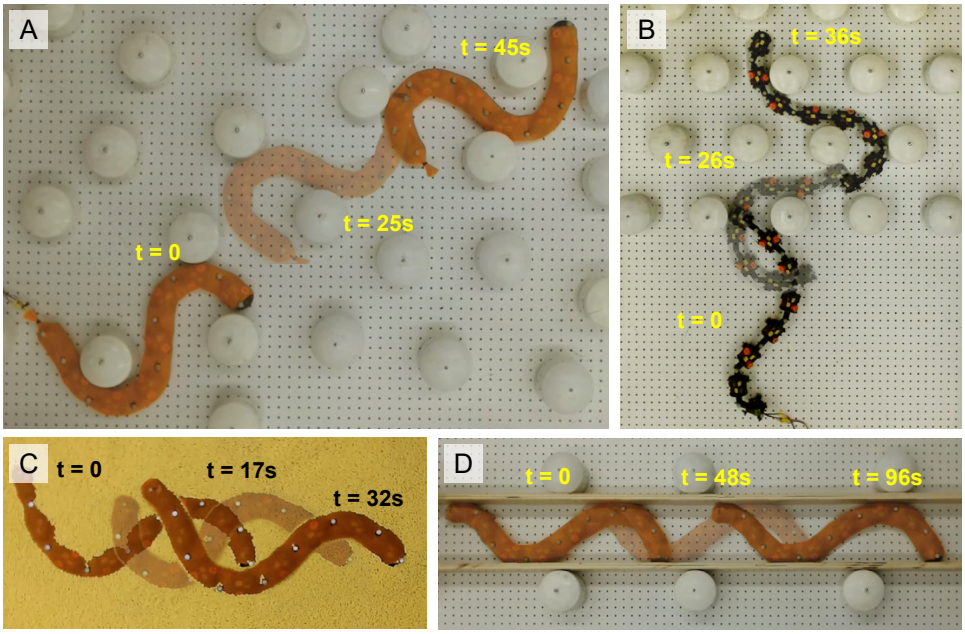

Fig. S11: Open-loop robotic terrestrial capabilities in various types of complex environments facilitated by mechanical intelligence. (**A**) The robot traverses a randomly distributed obstacle array. (**B**) The robot transitions from flat ground to a densely distributed obstacle array. (**C**) The robot locomotes in granular media (5 mm plastic spheres). (**D**) The robot moves in a narrow channel (18 cm width) formed with two parallel rigid walls.

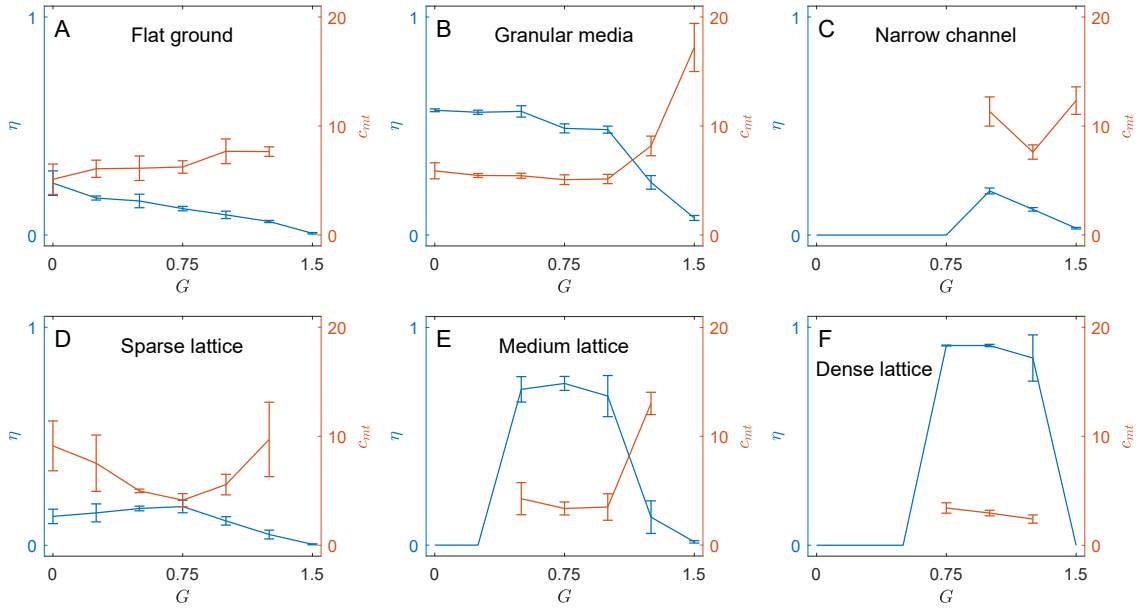

Fig. S12: Robot locomotion speed (wave efficiency, η) and mechanical cost of transport (c_{mt}) in different environments: (**A**) flat ground, (**B**) granular material (5 mm plastic spheres), (**C**) a narrow channel (18 cm width), (**D**) a sparse lattice, (**E**) a medium lattice, and (**F**) a dense lattice. Error bars represent standard deviations across three repetitive trials of each experiment.

Supplementary movie captions

Movie S1. *C. elegans* locomotion in heterogeneous terrain.

Movie S2. Overview of the robophysical model: the bilateral actuation mechanism and the programmable body compliance (generalized compliance G).

Movie S3. Robophysical locomotion with varied generalized compliance G.

Movie S4. Biological and robophysical locomotor performance comparison in all environments.

Movie S5. Biological and robophysical emergent locomotor behavior comparison.

Movie S6. Open-loop (without reversal) and closed-loop (with reversal) robophysical locomotion comparison.

Movie S7. Open-loop robotic terrestrial capabilities in complex laboratory environments, demon-

strating locomotion potentials in varied environments and to broad applications.

Movie S8. Open-loop robotic terrestrial capabilities in an example outdoor complex environment, a pile of irregular rocks, demonstrating the benefit of exploiting mechanical intelligence in real-world applications.